Journal of Power Sources 677 (2026) 239958



Contents lists available at ScienceDirect

Journal of Power Sources

journal homepage: www.elsevier.com/locate/jpowsour





Influence of sintering temperature on the performance of garnet-based all-solid-state Li-metal batteries

Zhizhen Qin [a,b,*], Jehad Ahmed [a,b], Dmitri L. Danilov [a,c], Baolin Wu [a], Anna Windmüller [a], Shicheng Yu [a], Chih-Long Tsai [a,**], Josef Granwehr [a], Chih-Chieh Wang [d], Rüdiger-A. Eichel [a,b], Peter H.L. Notten [a,c,e]

[a] Institute of Energy Technologies: Fundamental Electrochemistry (IET-1), Forschungszentrum Jülich GmbH, 52428, Jülich, Germany
[b] Institute of Physical Chemistry, RWTH Aachen University, 52074, Aachen, Germany
[c] Eindhoven University of Technology, P.O. Box 513, 5600 MB, Eindhoven, the Netherlands
[d] Department of Materials and Optoelectronic Science, National Sun Yat-sen University, Kaohsiung, 80424, Taiwan
[e] University of Technology Sydney, Broadway, Sydney, NSW, 2007, Australia

HIGHLIGHTS

- LCO/LLZO composite cathode was co-sintered onto LLZO to build ASSLMB.
- $<$ 895 °C, loose cathode structure, high impedance, fast capacity degradation.
- Higher sintering temperature, denser microstructure but severer side reactions.
- $\geq$ 995 °C, early battery failure, likely due to excessive stress.
- Side reaction byproduct Li-La-Co-O was identified by Raman-EDX-mapping and XRD.

ARTICLE INFO

Keywords:
All-solid-state Li-metal batteries
LLZO
Composite cathode
Sintering temperature
Side reactions
Microstructure

ABSTRACT

All-solid-state Li-metal batteries (ASSLMBs) based on $Li_7La_3Zr_2O_7$ (LLZO) solid electrolytes (SEs) are promising candidates for next-generation energy storage devices. Although the composite cathode obtained by sintering well-mixed $LiCoO_2$ (LCO) and LLZO at high temperature can overcome the problem of low ionic conductivity within the cathode, the capacity and cycling stability of such LLZO-based ASSLMBs are still not satisfactory. Systematically investigating the impact of sintering conditions on ASSLMB helps identify limiting factors and guides further optimization. Herein, we investigated the influence of sintering temperature on the phase composition, microstructure and electrochemical performance of LLZO-based ASSLMBs. It was found that low sintering temperature leads to a loose microstructure within the composite cathode, resulting in high impedance, low LCO utilization and rapid capacity degradation. Increasing the sintering temperature results in a denser composite cathode, thereby reducing impedance and improving cycling stability. Meanwhile, side reactions within the composite cathode become severer, lowering the initial Coulombic Efficiency (CE). Continuously increasing the sintering temperature ultimately leads to early battery failure, likely due to excessive stress in the overly dense cathode. Overall, our study shows that sintering temperature has multiple influences on the performance of LLZO-based ASSLMBs. Further performance optimization requires balancing trade-offs among multiple limiting factors.

1. Introduction

Currently, Li-ion batteries (LIBs) are ubiquitous in everyday life, found in smartphones, home appliances, robots, and automobiles [1,2]. However, with further development of modern society, the requirements for energy density and safety standards of energy storage

* Corresponding author. Institute of Energy Technologies: Fundamental Electrochemistry (IET-1), Forschungszentrum Jülich GmbH, 52428, Jülich, Germany.
** Corresponding author.
E-mail addresses: z.qin@fz-juelich.de (Z. Qin), c.tsai@fz-juelich.de (C.-L. Tsai).

https://doi.org/10.1016/j.jpowsour.2026.239958
Received 17 January 2026; Received in revised form 12 March 2026; Accepted 21 March 2026
Available online 25 March 2026
0378-7753/© 2026 The Authors. Published by Elsevier B.V. This is an open access article under the CC BY license (http://creativecommons.org/licenses/by/4.0/).

batteries are becoming increasingly stringent [3–6]. Therefore, the development of new types of secondary batteries is imperative.

Li-metal batteries (LMBs) have a significant advantage in energy density, with a theoretical energy density exceeding 500 Wh•kg^{-1}, far surpassing that of current commercial LIBs, which is only in the range of 250-300 Wh•kg^{-1} [7,8]. This improvement mainly stems from the high specific capacity (theoretically reaching 3860 mAh•g^{-1}), low density (0.53 g•cm^{-3}), and low electrochemical potential (−3.04 V *vs.* Standard Hydrogen Electrode) of the Li-metal anode [9,10]. However, in terms of safety, the bad compatibility between traditional liquid electrolytes and Li-metal presents more serious safety risks [11,12]. For example, side reactions between liquid electrolytes and Li-metal anode not only lead to the consumption of both components, resulting in continuous capacity degradation and uncontrollable growth of the solid electrolyte interphase (SEI), but also generate a large amount of heat, potentially triggering thermal runaway [13–15]. Besides, LMBs are more prone to Li-dendrite formation due to defects on the Li-metal surface, insufficient mechanical stability of the SEI layer, or excessive current density, which can eventually cause short-circuit [16,17]. Furthermore, the large volume change of Li-metal causes the break of the SEI layer, exposing fresh Li-metal surfaces to form new hot spots for Li-dendrite, which continuously facilitates the two harmful processes mentioned above until battery failure, or in more severe cases, until fires and explosions [18–20]. To improve the safety of LMBs, researchers have proposed many strategies, such as liquid electrolyte engineering [21–23], artificial SEI layers [24–26], and structure design of Li-metal anode [27,28]. However, these strategies fall short when faced with more stringent testing conditions, such as thermal testing and nail penetration experiments.

ASSLMBs, which use SEs instead of liquid electrolytes, effectively eliminate the risk of fire and explosion caused by organic liquids, thereby offering inherent safety [29,30]. Among all kinds of SEs, LLZO-based SEs outstand due to their wide electrochemical window, good electrochemical and mechanical stability against Li-metal anode and good ionic conductivity [31–33]. Extensive research about LLZO itself and the Li/LLZO interface has further improved the ionic conductivity of LLZO [34,35], reduced the Li/LLZO interfacial impedance [36,37], and suppressed Li-dendrite formation [38]. However, due to the low ionic conductivity of the cathode material, LLZO-based ASSLMBs, like other ASSLMBs, often experience ion transport limitations within the cathode, hindering the full capacity release and limiting the loading of cathode active materials. To overcome this common disadvantage, a composite cathode composed of well-mixed cathode active material and SE was proposed to enable ASSLMBs [39,40]. Sulfide-based composite cathodes are typically fabricated by mixing a cathode active material with sulfide SE particles and other additives (if needed), followed by cold or warm pressing (<250 °C) under a high pressure of hundreds of MPa to form a dense composite cathode layer [41,42]. To prepare a polymer-based composite cathode, the polymer binder, Li-salt, and cathode active material are first dissolved in a solvent, and then ball milling or stirring is conducted to improve the dispersion uniformity. Finally, the solvent is completely dried under vacuum conditions [43,44]. Unlike sulfide- and polymer-based ASSLMBs, high-temperature sintering is often required to promote the contact between LLZO and cathode active material due to their high rigidity [45]. Thanks to its chemical stability with LLZO at high temperature and its similar thermal expansion coefficient to LLZO, LCO has become the most suitable material for constructing LLZO-based composite cathodes [46–48]. Tsai et al. built an LCO-LLZO||LLZO||Li-In ASSLMB with high LCO loading by sintering the composite cathode onto the LLZO over 1000 °C. However, the ASSLMB showed rapid capacity degradation during cycling with only 25% initial capacity left after 100 cycles [49]. By further improving the microstructure of the LCO/LLZO composite cathode, a LCO-LLZO||LLZO||Li ASSLMB sintered at 970 °C was reported, which showed an initial charging capacity of 1.0 mAh•cm^{-2} and a remained capacity of 0.51 mAh•cm^{-2} after 100 cycles [50]. In fact, most of the capacity was lost during 1st cycle as the 1st CE was only 63%. Ihrig et al. demonstrated the potential of the pressure-supported field-assisted sintering technique (FAST). A LCO-LLZO||LLZO||Li-In ASSLMB was prepared under a high mechanical pressure (440 MPa) and a low sintering temperature (750 °C), which showed high initial charging and discharging capacity of 1.15 and 0.9 mAh•cm^{-2}, respectively. However, after 45 cycles, only about 0.3 mAh•cm^{-2} capacity was left [51].

Despite researchers' efforts, the capacity retention and cycling stability of LLZO-based ASSLMBs remain unsatisfactory. Systematic optimization of the sintering process and understanding the impact of each sintering parameter on ASSLMBs are key to identifying directions for further improving ASSLMB performance. In this study, LCO/LLZO composite cathodes were sintered onto LLZO SEs under air at different sintering temperatures to understand the comprehensive influence of sintering temperature on LLZO-based ASSLMBs. The cross-section of these sintered composite cathodes was tested by Raman mapping combined with EDX mapping to understand the influence of sintering temperature on the phase composition. Then, SEM was used to study the influence of sintering temperature on the microstructure within the composite cathode. Finally, electrochemical measurements were conducted to show the influence of sintering temperature on the electrochemical performance of LLZO-based ASSLMBs.

2. Experimental

2.1. Preparation of ASSLMBs

The preparation of the ASSLMBs was the same as our previous work [52]. Here, only a brief description is provided.

LLZO-based SE: $Li_{6.45}Al_{0.05}La_3Zr_{1.6}Ta_{0.4}O_{12}$ was prepared by solid-state reaction using well-mixed precursors: LiOH•H_2O (Merck, 98%), La_2O_3 (Merck, 99.9%, pre-dried at 900 °C for 10 h), ZrO_2 (Treibacher, 99.5%), Ta_2O_5 (Inframat, 99.95%), and α-Al_2O_3 (Inframat, 99.9%). The powder mixture went through three calcination steps: once at 850 °C and twice at 1000 °C, each for 20 h, followed by a sintering process at 1175 °C for 10 h. Grinding, mixing, and pressing into pellets were repeated before each heating step to ensure high uniformity in the final product. After sintering, LLZO pellets were sliced and polished to get discs with a thickness of ≈600 μm.

Composite cathode ink: mixed powder was prepared by ball milling LCO (MTI Corp., USA) and LLZO powder with a mass ratio of 1:1. Then equal masses of mixed powder and a terpineol (Sigma-Aldrich) solvent containing 3 wt% ethyl cellulose (Sigma-Aldrich) were mixed using a three-roll milling to obtain a uniform composite cathode ink.

ASSLMBs: a certain amount of composite cathode ink was hand-brushed onto one side of the LLZO disc. After that, the sample was sintered in a tube furnace (Nabertherm, Germany) under an air atmosphere at the required temperatures, with a dwell time of 15 min. After sintering, the anode side was polished again and coated with an Au interlayer. The ASSLMB was obtained after Li was attached to the anode side in the glovebox. The fabricated ASSLMB was also heated to 250 °C to further improve the contact between LLZO and the Li anode. Then the ASSLMB was placed in a Swagelok cell, and a spring was used within the cell to apply a pressure of 0.1 MPa.

All the fabricated ASSLMBs have similar LCO loading in the range of 6.5∼7.0 mg•cm^{-2}. Since different sintering temperatures, i.e., 895, 920, 945, 970, and 995 °C, were used, the obtained ASSLMBs were named A895, A920, A945, A970, and A995, respectively.

2.2. Electrochemical performance

A multi-potentiostat (BioLogic VMP-300) combined with a climate chamber (Maccor, Inc., USA) set to 60 °C was used to conduct the electrochemical measurements of all ASSLMBs. During charging, a constant current density of 50 μA•cm^{-2} was applied until the voltage

reached 4.2 V *vs.* Li/Li^+, after which a constant voltage was applied until the current density declined to 10 μA•cm^{-2}. During discharging, a constant current density of 50 μA•cm^{-2} was applied until the voltage reached 3.4 V *vs.* Li/Li^+. After 1st charging of each ASSLMB, the electrochemical impedance spectroscopy (EIS) test was conducted at a frequency range of 7 MHz to 1 Hz with a perturbation AC amplitude of 10 mV.

2.3. Characterizations

Raman mapping combined with EDX mapping was carried out using a Zeiss-RISE (Raman Imaging and Scanning Electron Microscopy). Raman microscopy was performed using a 532 nm excitation laser and 600 g•mm^{-1} grating, with a laser power of 1.0 mW. The spectra were collected for an area of 20 μm × 20 μm with a step size of (x, y) = (0.357 μm, 0.5 μm) and a 3 s spectral acquisition time. The total number of acquired spectra for the mapping was 2240. The mappings were processed within the WITec Project 6.2 Software using cosmic-ray removal and background noise subtraction. The method used for background subtraction is based on approaching a rounded shape to the spectrum. The mapping was analyzed using the TrueComponent Analysis within the WITec Project 6.2 software, which identifies components and generates intensity distribution images of them. The EDX mapping was then collected at the same test area with an accelerating voltage of 20 kV and a scan rate of 45 μs^{-1}.

SEM experiments were conducted to investigate the microstructure, using a Quanta FEG 650 (FEI) environmental scanning electron microscope. All investigations were performed with the e-beam at 20 kV.

3. Result and discussion

As shown in Fig. 1, the cross-sections of A895, A945, and A995 were analyzed by Raman mapping combined with EDX mapping to investigate the influence of sintering temperature on side reactions. Two phases were observed in the composite cathode of A895 (Fig. 1a): LCO (red) and LLZO (green). In the average Raman spectrum of the red phase, Fig. 1b, three characteristic peaks belonging to LCO are observed at 484, 595, and 1176 cm^{-1}, which can be attributed to the O-Co-O bending mode, Co-O stretching mode, and overtone of the Co-O stretching mode, respectively [53,54]. The additional peak present at

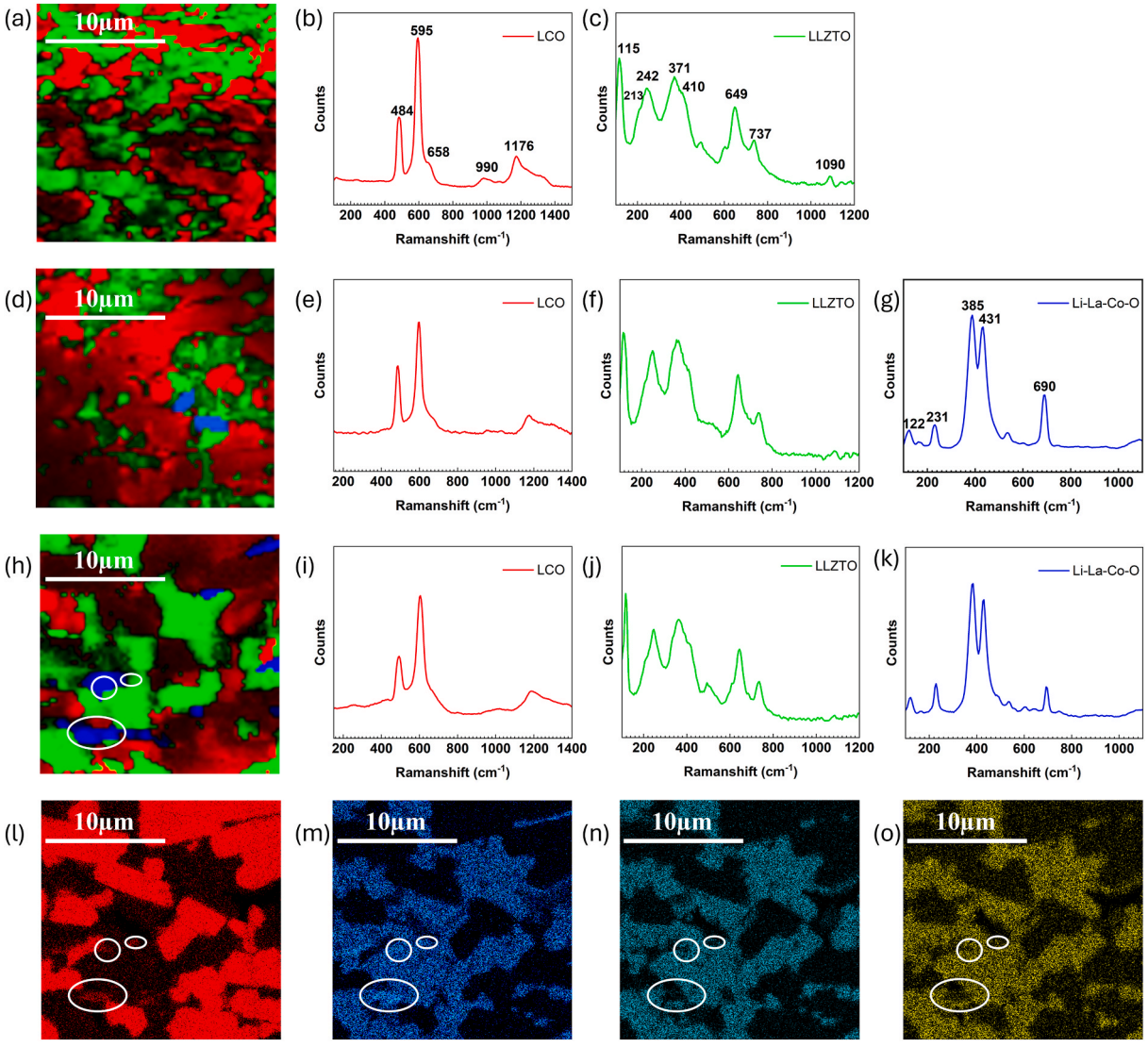

Fig. 1. Raman-EDX mapping of the cross-section of A895, A945, and A995. The results from A895 for its (a) Raman mapping and (b), (c) analyzed average Raman spectra for LCO and LLZO phase, respectively. The results from A945 for its (d) Raman mapping and (e) - (g) analyzed average spectra for LCO, LLZO, and possible impurity phase, respectively. The results from A995 for its (h) Raman mapping; (i) - (k) analyzed average spectra for LCO, LLZO, and possible impurity phase, respectively; (l) - (o) EDX mapping of Co, La, Zr, and Ta, respectively.

990 cm^{-1} was also reported in the spectrum of LCO in the literature [54]. The peak at 658 cm^{-1} can be attributed to the characteristic of the octahedral sites (CoO_6) belonging to Co_3O_4, an impurity likely inherited from the pristine LCO material [49,55]. The average Raman spectrum of the green phase is shown in Fig. 1c which indicates predominantly cubic LLZO phase rather than tetragonal LLZO phase, as evidenced by the presence of two shoulder peaks around 213 and 410 cm^{-1} and two broad peaks at 242 and 371 cm^{-1} instead of sharp peaks around 209, 291, 346, 370, and 404 cm^{-1} [56,57]. The peak at 649 cm^{-1} represents the vibrational stretching modes of the Zr-O bond [58]. Furthermore, the peak at 737 cm^{-1} corresponds to the stretching of TaO_6 octahedra, confirming the partial substitution of Zr by Ta [59]. There is a small impurity peak at 1090 cm^{-1} representing a low content of the Li_2CO_3 phase which is caused by the proton-exchange reaction of LLZO [60,61]. The assignment of characteristic peaks of LCO and LLZO are summarized in Table S1.

Within the cross-section of A945, Fig. 1d, a total of 3 phases can be distinguished. In addition to LCO (red) and cubic LLZO (green) phases, Fig. 1e and f, another impurity phase (blue) characterized by the strong peaks at 385, 431, and 690 cm^{-1} appeared, Fig. 1g. Within the cross-section of A995, Fig. 1h–k, the phase composition was the same as that of A945, but the impurity phase content appeared to be higher. This impurity phase was also observed in our previous study [52]. By comparing with all possible impurities commonly seen in this system, we attributed this phase to the $Li_{0.5}La_2Co_{0.5}O_4$ species, which shows similar peaks at 371, 425, and 685 cm^{-1} in the literature [62]. Here, we further confirm this idea by comparing Raman and EDX mapping in the same test area. Fig. 1l–o shows the single element EDX mapping of Co, La, Zr, and Ta, respectively, in the same testing region as in Fig. 1h. Although the shape of Raman and EDX mapping is difficult to match perfectly due to resolution limitations, image drifting and processing of Raman mapping, we can still find some spots (marked by white circles in different shapes) to confirm that the impurity phase is Co- and La-rich but contains no Zr and Ta. By comparing Raman mapping of different ASSLMBs, it can be concluded that the content of $Li_{0.5}La_2Co_{0.5}O_4$ gets higher with higher sintering temperatures. This conclusion is also supported by XRD measurements which performed on the top surface of the sintered composite cathodes, as shown in Fig. S1. Besides, since the preparation process of these ASSLMBs was conducted in air, the Li_2CO_3 phase was inevitably formed by proton-exchange reaction of LLZO. However, regardless of the sintering temperature, its content in the bulk phase remains relatively low as shown by the small peak at 1090 cm^{-1} in Fig. 1c, f, and j.

The cross-sections of different ASSLMBs, Fig. 2, were investigated by SEM to examine the influence of sintering temperature on the microstructure of the composite cathodes. In A895, Fig. 2a, there were many pores within the composite cathode, sized from few micrometers to over 10 μm, and many voids can be seen at the interface between the composite cathode and SE. As the sintering temperature gradually increased to 995 °C, Fig. 2b–e, the microstructure of composite cathode generally became denser with less and smaller pores within the composite cathode. The SEM images were processed by python using Gaussian Kuwahara filters to obtain their porosities. As shown in Fig. S2, the calculated porosities of these composite cathodes decreased from 16% to 3.6% when sintering temperature generally increased from 895 to 995 °C. Lower porosity means better connection between particles, which favors the movement of ions and electrons within the composite cathode. Besides, the connection between the composite cathode and SE also became tighter with fewer voids in between, facilitating ion transport across the interface.

However, increasing the sintering temperature is not always beneficial to the microstructure. For example, the agglomeration of LLZO particles also increased with higher sintering temperature, as most of the LLZO agglomerates in A895 only have a radius of a few micrometers, while those in A995 can reach a radius of up to tens of micrometers. Over-agglomeration may affect the distribution of LLZO particles, potentially leading to an insufficient ion-percolation network. Besides, according to Yu et al., [63] since LLZO has a larger coefficient of thermal expansion than LCO, the shrinkage of LLZO during cooling is greater than that of LCO. Therefore, LCO is subject to compressive stress from the matrix within the composite cathode. Increasing the sintering temperature amplifies this stress. In addition, Han et al., [64] also revealed that residual stress on the cathode active material plays a pivotal role in degradation during cycling.

After identifying the phase composition and microstructure, electrochemical tests were performed to understand the impact of sintering temperatures on the performance of ASSLMBs. Fig. 3 shows the first electrochemical cycle of all the ASSLMBs sintered at different temperatures. The ASSLMB sintering at 895 °C showed a low charging capacity of 0.95 mAh•cm^{-2}, a high capacity loss of 0.30 mAh•cm^{-2}, and thus a low 1st CE of 68.5%. The EIS test after the 1st charging showed that A895 had a high total impedance of 795.5 Ω cm^2. The poor performance of A895 may relate to the porous structure of the composite cathode, as shown in Fig. 2a, where LCO and LLZO particles are loosely connected, resulting in a low cathode active material utilization and a high impedance across the LCO/LLZO interface, as supported by the

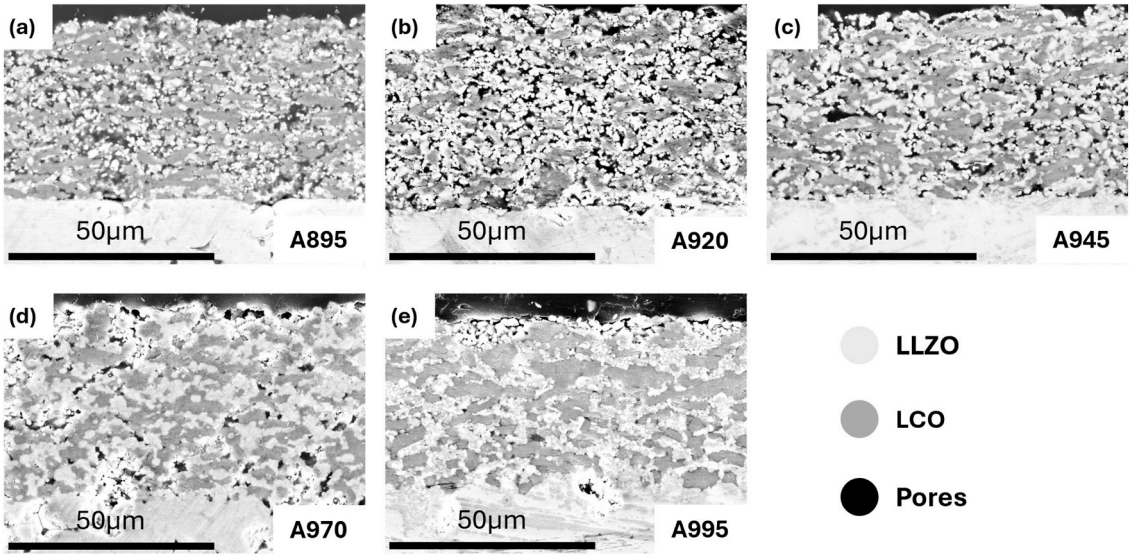

Fig. 2. SEM images of the composite cathode microstructures of (a) A895, (b) A920, (c) A945, (d) A970, (e) A995.

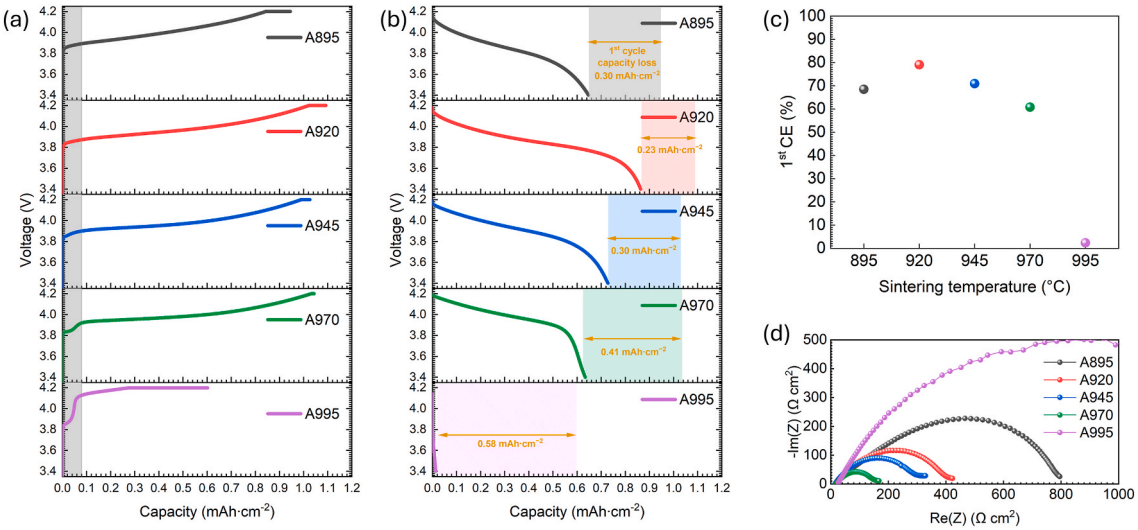

Fig. 3. First electrochemical cycle performance of all the ASSLMBs sintered at different temperatures. a) first charging curves b) first discharging curves c) first cycle CE, d) EIS after first charging.

equivalent circuit fitting in Fig. S3 and Table S2. When the sintering temperature increased from 895 to 920 °C, the A920 showed a much higher charging capacity of 1.09 mAh•cm^{-2} and a relatively lower capacity loss of 0.23 mAh•cm^{-2} leading to a 1st CE of 79.1%. The total impedance after the 1st charging decreased to 422.9 Ω cm^2. When the sintering temperature further increased from 920 to 970 °C, on the one hand, the 1st charging capacity of ASSLMBs no longer increased, indicating that the microstructure established above 920 °C already provided a sufficient LCO utilization. On the other hand, the overall impedance further decreased as shown in Fig. 3d, which can be attributed to the denser microstructure within the composite cathode and to the better connection between composite cathode and SE as shown in Fig. 2b–d. The EIS result is also consistent with the different shapes of the discharging curves of these ASSLMBs, Fig. 3b. The discharging curves of A920 and A945 are more roundish in shape while that of A970 shows a steep down of voltage when reaching ~3.8 V *vs.* Li/Li$^+$, which belongs to the typical LCO discharging behavior. This observation indicates that the A970 exhibited lower battery polarization compared to A920 and A945.

Surprisingly, despite improvements in microstructure and impedance, the capacity loss during 1st cycle increased, and the 1st CE decreased with increased sintering temperature from 920 to 970 °C. This phenomenon may partially relate to the appearance of an additional charging plateau between 3.8 V and 4.0 V *vs.* Li/Li$^+$, which became larger at higher sintering temperatures, Fig. 3a. There is no corresponding discharging plateau in Fig. 3b, thus such a charging plateau is likely due to irreversible electrochemical decomposition of a certain substance, which contributes to a capacity loss during 1st cycle. The LLZO-based ASSLMBs sintered under an oxygen atmosphere also showed the same plateau which ruled out the possibility that this plateau is caused by oxygen deficiency or is originated from Li_2CO_3 or other impurities resulting from proton exchange reactions, such as LiOH, Li_xO_y [52]. Furthermore, according to the Raman mapping results in Fig. 1, the content of Li_2CO_3 did not increased with higher sintering temperature thus could not cause a larger decomposition plateau. The recent research by Din et al. showed that Co incorporated LLZO shows an irreversible oxidation peak at 4.0 V *vs.* Li/Li$^+$ in the CV test [65]. They hypothesized that this peak could come from another Li-La-Co-O species, $LiLa_{0.95}Co_{0.26}O_2$, found in the Co incorporated LLZO or the destabilization of LLZO caused by Co diffusion. Although the exact impurities responsible for this plateau remain controversial, our work has demonstrated that the occurrence of corresponding side reactions or element diffusion can be controlled by lowering the sintering temperature. Besides, microstructural degradation is another possible factor contributing to capacity loss during the 1st cycle, as A895 and A920, which do not contain observable impurities, also showed unsatisfactory 1st CE. Furthermore, after excluding the impact of this plateau, the A970 suffered a greater capacity loss, around 0.33 mAh•cm^{-2}, than the A920, less than 0.23 mAh•cm^{-2}, which supports the idea that increasing the sintering temperature may also have an adverse effect on the microstructure, for example stronger LLZO aggregation and larger structural stress as mentioned above.

When the sintering temperature further increased to 995 °C, the ASSLMB could not be charged or discharged normally. The extremely high capacity loss during the 1st cycle and the impedance observed after the 1st charging indicate that the microstructure of A995 may have been damaged during the 1st charging due to the large stress caused by its overly dense microstructure which lacks free space to accommodate the volume change of LCO [52,64].

Long-term electrochemical cycling was performed to investigate the cycling stability of ASSLMBs sintered at different temperatures in air. As shown in Fig. 4a, A895 not only exhibited a low initial discharging capacity of 0.65 mAh•cm^{-2} but also a rapid capacity degradation with a low average CE of 98.8% after the 1st cycle. After 50 cycles, the capacity of A895 reduced to only 0.38 mAh•cm^{-2}. Although, A920 showed the highest initial discharging capacity of 0.86 mAh•cm^{-2}, it also exhibited rapid capacity degradation with an average CE of 98.6% after the 1st cycle and a capacity of 0.47 mAh•cm^{-2} after 50 cycles. When the sintering temperature increased to 945 °C, A945 showed an initial discharging capacity of 0.73 mAh•cm^{-2}, which was lower than that of A920, but its cycling stability was improved. It retained a discharging capacity of 0.54 mAh•cm^{-2} after 50 cycles with an average CE of 99.2% after 1st cycle. When the sintering temperature was further increased to 970 °C, although the initial discharging capacity further decreased to 0.63 mAh•cm^{-2}, the cycling stability improved with a discharging capacity of 0.57 mAh•cm^{-2} after 50 cycles and an average CE of 99.4 % after the 1st cycle. In general, the cycling stability of ASSLMB was improved when the sintering temperature increased from 895 to 970 °C.

It is known that microstructure degradations including LCO/LLZO delamination and trans- and inter-granular cracks caused by stress, are the main reasons for the capacity degradation of this type of ASSLMBs [50,52,64]. Considering the density of the initial microstructure of these ASSLMBs, Fig. 2, the fast capacity degradation of A895 and A920 can be attributed mainly to the delamination between the LCO/LLZO interface. The charging/discharging curves over cycling for ASSLMBs are shown here to provide additional information related to capacity degradation.

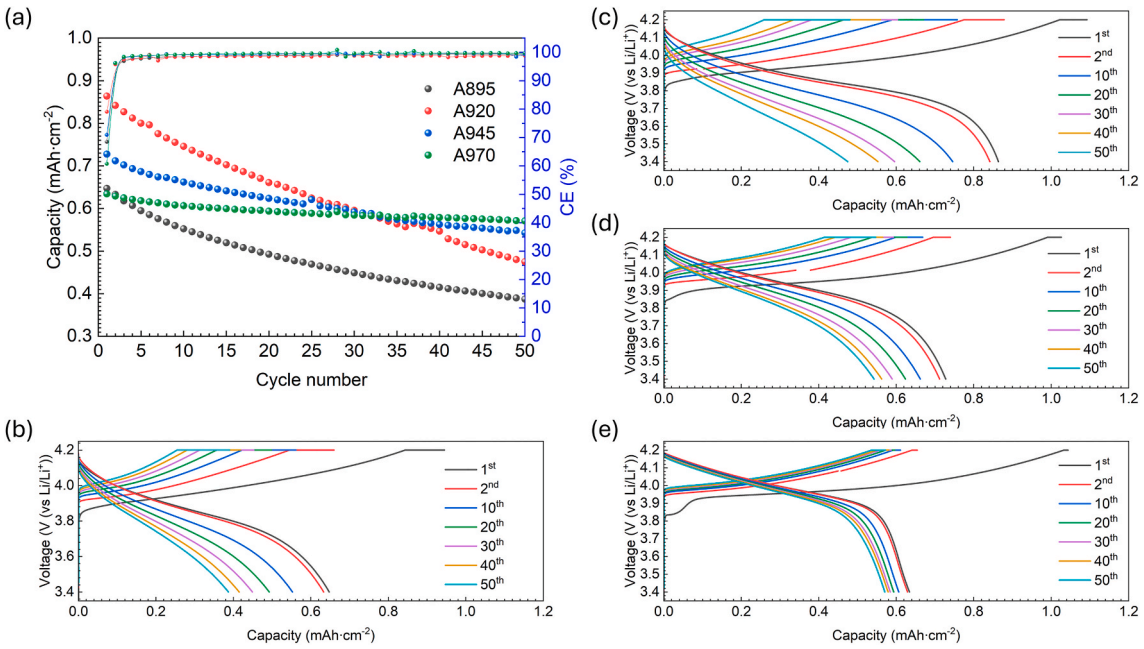

Fig. 4. Long-term cycle performance of ASSLMBs with a current of 50 μA•cm^{-2} at 60 °C between 3.4 and 4.2 V *vs.* Li/Li^{+}. (a) Long-term cycling performance of the discharging areal capacity and Coulombic efficiency versus cycle number; long-term charging/discharging curves for (b) A895, (c) A920, (d) A945, and (e) A970.

It can be seen from Fig. 4b and c, for A895 and A920, the capacity from the constant-current charging regime decreased rapidly with increasing cycle number, whereas that from the constant-voltage charging regime apparently increased. This phenomenon indicates a significant increase in polarization. A similar conclusion can be drawn from the changes in their discharging curves which developed from convex to linear with increasing cycle number. The enhanced polarization indicates longer ion or electron transport paths, supporting the idea that their capacity degradation is mainly caused by delamination within the composite cathode. For A945, Fig. 4d, the increase in polarization became slower as demonstrated by the slower decrease of the constant-current charging capacity and increase of the constant-voltage charging capacity. After 50 cycles, the discharging curve of A945 still showed convex shape. In contrast, for A970 (Fig. 4e) the changes in constant-current and constant-voltage charging capacities during cycling were very limited. More importantly, its discharging curves over 50 cycles maintained a stable shape, showing a steep drop at ~3.8 V *vs.* Li/Li^{+}, which indicates a minor increase in polarization for A970. The better cycling stability of A945 and A970 is likely due to their denser initial microstructure, which helps to maintain stability during cycling and mitigates the delamination between LCO and LLZO. However, the influence of structural stress should not be ignored. A995 has an even denser initial microstructure, which should be able to further suppress the delamination. However, it failed at an early stage, likely due to the significant stress accumulated within the composite cathode, as discussed above.

4. Conclusion

A series of LLZO-based ASSLMBs were prepared by sintering the composite cathode under air at different sintering temperatures to investigate the influence of sintering temperature on the composition, the microstructure, and eventually the electrochemical performance of these ASSLMBs.

According to the phase identification, higher sintering temperature can lead to severer side reactions. In addition to the LCO and LLZO phases, an impurity phase was found in the composite cathode when sintering temperature excesses 945 °C, and its content increased with higher sintering temperature. According to the results of Raman and EDX mapping from the same testing area, this impurity is likely $Li_{0.5}La_2Co_{0.5}O_4$ or a similar Li-La-Co-O species.

SEM images of prepared ASSLMBs showed that, with higher sintering temperature, the microstructure of composite cathode became denser and the connection between composite cathode and SE became better. Meanwhile, the agglomeration of LLZO particles also seemed to be stronger.

Electrochemical tests showed the changes in ASSLMB performance with increasing temperature:

(1) Under low sintering temperature, 895 °C, the resulting composite cathode could not provide sufficient LCO utilization and showed high impedance due to insufficient connections between LCO and LLZO, and also between the composite cathode and SE.
(2) When the sintering temperature reached 920 °C, the LCO utilization and 1st CE increased. At the same time, the cell impedance decreased, which can be attributed to the increase in density of the composite cathode and better connection between composite cathode and SE.
(3) By further increasing the sintering temperature to 970 °C, although the cell impedance continued to decrease, LCO utilization no longer increased, and the 1st CE became lower. The lower 1st CE can be partially attributed to side reactions during sintering. When the sintering temperature exceeded 945 °C, an additional irreversible charging plateau appeared in the first charging and grew larger with higher sintering temperature. This plateau may be related to the irreversible electrochemical decomposition of Li-La-Co-O impurities or destabilized LLZO caused by Co diffusion during sintering as supported by the research of Din et al. Additionally, unfavorable factors related to the microstructure also contribute to the lower 1st CE.
(4) When the sintering temperature reached 995 °C, the ASSLMB failed during 1st charging, probably because of the huge stress caused by the overly dense microstructure.
(5) Long-term cycling results showed that when the sintering temperature increased from 895 to 970 °C, the cycling stability of the ASSLMB generally increased. The improvement in cycling stability can also be attributed to the increased density of the initial microstructure which suppressed the delamination between LCO

and LLZO during cycling, thus mitigating the growth of cell impedance.

In summary, this work investigates how sintering temperature influences the composition and microstructure of the composite cathode of LLZO-based ASSLMBs, including the extent of side reactions and element diffusion, the density, LLZO particle aggregation, and structural stress. Competition among these factors leads to considerable differences in the electrochemical performance of these ASSLMBs. Therefore, to achieve better performance of ASSLMBs, it is necessary to balance these factors. One feasible approach is lowering the sintering temperature to suppress side reactions, meanwhile, further optimizing the microstructure of the composite cathode to ensure close contact between particles and high LCO utilization, for example, by optimizing the particle size and dispersion of LLZO particles or by adding sintering additives.

CRediT authorship contribution statement

Zhizhen Qin: Writing – original draft, Methodology, Investigation, Formal analysis, Data curation. **Jehad Ahmed:** Investigation. **Dmitri L. Danilov:** Writing – review & editing, Supervision. **Baolin Wu:** Investigation. **Anna Windmüller:** Writing – review & editing. **Shicheng Yu:** Writing – review & editing. **Chih-Long Tsai:** Writing – review & editing, Supervision, Methodology. **Josef Granwehr:** Funding acquisition. **Chih-Chieh Wang:** Writing – review & editing, Funding acquisition. **Rüdiger-A. Eichel:** Project administration, Funding acquisition. **Peter H.L. Notten:** Writing – review & editing.

Declaration of competing interest

The authors declare that they have no known competing financial interests or personal relationships that could have appeared to influence the work reported in this paper.

Acknowledgements

The author Zhizhen Qin gratefully acknowledges fellowship support from the China Scholarship Council. The authors also would like to acknowledge the financial support by the project of “High-Performance Solid-State Batteries” (HIPSTER) from Ministeriumfür Kultur und Wissenschaft des Landes Nordrhein-Westfalen and project of AdamBatt2 (13XP0558A) from Bundesministerium für Forschung, Technologie und Raumfahrt (BMFTR) for DE-TW battery cooperation and project of National Science and Technology Council (NSTC) of Taiwan under contracts NSTC 111-2628-E-110-008- MY3 and NSTC 112-2923-E-006-004.

Appendix A. Supplementary data

Supplementary data to this article can be found online at https://doi.org/10.1016/j.jpowsour.2026.239958.

Data availability

Data will be made available on request.

References

[1] Y. Miao, P. Hynan, A. von Jouanne, A. Yokochi, Current Li-Ion battery technologies in electric vehicles and opportunities for advancements, Energies 12 (6) (2019) 1074.
[2] M. Li, J. Lu, Z. Chen, K. Amine, 30 years of lithium-ion batteries, Adv. Mater. 30 (33) (2018) 1800561.
[3] H. Niu, N. Zhang, Y. Lu, Z. Zhang, M. Li, J. Liu, N. Zhang, W. Song, Y. Zhao, Z. Miao, Strategies toward the development of high-energy-density lithium batteries, J. Energy Storage 88 (2024) 111666.
[4] F.M.N.U. Khan, M.G. Rasul, A.S.M. Sayem, N.K. Mandal, Design and optimization of lithium-ion battery as an efficient energy storage device for electric vehicles: a comprehensive review, J. Energy Storage 71 (2023) 108033.
[5] S. Awasthi, A review on the optimization of electrolytes to enhance lithium-ion batteries' safety and performance under abuse conditions, J. Energy Storage 100 (2024) 113439.
[6] W. Cao, J. Zhang, H. Li, Batteries with high theoretical energy densities, Energy Storage Mater. 26 (2020) 46.
[7] S. Chen, F. Dai, M. Cai, Opportunities and challenges of high-energy lithium metal batteries for electric vehicle applications, ACS Energy Lett. 5 (10) (2020) 3140.
[8] J. Liu, Z. Bao, Y. Cui, E.J. Dufek, J.B. Goodenough, P. Khalifah, Q. Li, B.Y. Liaw, P. Liu, A. Manthiram, Y.S. Meng, V.R. Subramanian, M.F. Toney, V. V. Viswanathan, M.S. Whittingham, J. Xiao, W. Xu, J. Yang, X.-Q. Yang, J.-G. Zhang, Pathways for practical high-energy long-cycling lithium metal batteries, Nat. Energy 4 (3) (2019) 180.
[9] P. Shi, X.-Q. Zhang, X. Shen, R. Zhang, H. Liu, Q. Zhang, A review of composite lithium metal anode for practical applications, Adv. Mater. Technol. 5 (1) (2020) 1900806.
[10] Z.A. Ghazi, Z. Sun, C. Sun, F. Qi, B. An, F. Li, H.-M. Cheng, Key aspects of lithium metal anodes for lithium metal batteries, Small 15 (32) (2019) 1900687.
[11] S.-J. Tan, W.-P. Wang, Y.-F. Tian, S. Xin, Y.-G. Guo, Advanced electrolytes enabling safe and stable rechargeable Li-Metal batteries: progress and prospects, Adv. Funct. Mater. 31 (45) (2021) 2105253.
[12] S. Li, M. Jiang, Y. Xie, H. Xu, J. Jia, J. Li, Developing high-performance lithium metal anode in liquid electrolytes: challenges and progress, Adv. Mater. 30 (17) (2018) 1706375.
[13] Y. Jie, X. Ren, R. Cao, W. Cai, S. Jiao, Advanced liquid electrolytes for rechargeable Li metal batteries, Adv. Funct. Mater. 30 (25) (2020) 1910777.
[14] X. Cui, J. Wang, S. Sun, X. Chen, Y. Wang, D. Han, J. Wang, X. Yao, W. Yan, Safety hazards of lithium metal batteries: from the perspective of lithium dendrites and thermal runaway, Energy Fuels 39 (16) (2025) 7665.
[15] Q.-K. Zhang, X.-Q. Zhang, H. Yuan, J.-Q. Huang, Thermally stable and nonflammable electrolytes for lithium metal batteries: progress and perspectives, Small Sci. 1 (10) (2021) 2100058.
[16] X. Zhang, A. Wang, X. Liu, J. Luo, Dendrites in lithium metal anodes: suppression, regulation, and elimination, Acc. Chem. Res. 52 (11) (2019) 3223.
[17] X. Gao, Y.-N. Zhou, D. Han, J. Zhou, D. Zhou, W. Tang, J.B. Goodenough, Thermodynamic understanding of Li-Dendrite formation, Joule 4 (9) (2020) 1864.
[18] H. Ye, Y. Zhang, Y.-X. Yin, F.-F. Cao, Y.-G. Guo, An outlook on low-volume-change lithium metal anodes for long-life batteries, ACS Cent. Sci. 6 (5) (2020) 661.
[19] J.-F. Ding, R. Xu, C. Yan, B.-Q. Li, H. Yuan, J.-Q. Huang, A review on the failure and regulation of solid electrolyte interphase in lithium batteries, J. Energy Chem. 59 (2021) 306.
[20] Y. Cheng, L. Jiang, X. Hu, Z. Yang, H. Xu, B. Kong, Y. Deng, L. Han, M. Zhang, X. Wei, Q. Wang, Fire safety challenge of lithium metal batteries and advanced strategies for improving intrinsic safety, J. Energy Chem. 110 (2025) 311.
[21] Z. Qin, B. Wu, D.L. Danilov, R.-A. Eichel, P.H.L. Notten, Dual-salts electrolyte with fluoroethylene carbonate additive for high-voltage Li-metal batteries, Batteries 9 (9) (2023).
[22] H. Wang, Z. Yu, X. Kong, S.C. Kim, D.T. Boyle, J. Qin, Z. Bao, Y. Cui, Liquid electrolyte: the nexus of practical lithium metal batteries, Joule 6 (3) (2022) 588.
[23] N. Li, X. Han, X. Cui, C. Xu, C. Mao, X. Dai, W. Xue, Recent progress in liquid electrolytes for high-energy lithium–metal batteries: from molecular engineering to applications, Adv. Funct. Mater. 35 (1) (2025) 2409431.
[24] Y. Zhang, Z. Wei, X. Yuan, Y. Qiu, Y. Cai, L. Xu, H. Zhang, Recent progress of artificial SEI for high-energy lithium batteries: mechanisms, fabrication strategies and structure-performance relationships, Nano Energy 142 (2025) 111219.
[25] H. Song, J. Lee, M. Sagong, J. Jeon, Y. Han, J. Kim, H.-G. Jung, J.-S. Yu, J. Lee, I.-D. Kim, Overcoming chemical and mechanical instabilities in lithium metal anodes with sustainable and eco-friendly artificial SEI layer, Adv. Mater. 36 (47) (2024) 2407381.
[26] S. Burger, J. Skrotzki, J. Büttner, W. Beichel, P. Klose, A. Welle, A. Fischer, I. Krossing, Toward realistic full cells with protected lithium-metal-anodes: the effect of an adaptive self-healing artificial SEI, Adv. Energy Mater. 15 (13) (2025) 2403195.
[27] Y. Zhao, X. Yang, Q. Sun, X. Gao, X. Lin, C. Wang, F. Zhao, Y. Sun, K.R. Adair, R. Li, M. Cai, X. Sun, Dendrite-free and minimum volume change Li metal anode achieved by three-dimensional artificial interlayers, Energy Storage Mater. 15 (2018) 415.
[28] S. Matsuda, Y. Kubo, K. Uosaki, S. Nakanishi, Insulative microfiber 3D matrix as a host material minimizing volume change of the anode of Li metal batteries, ACS Energy Lett. 2 (4) (2017) 924.
[29] D.H.S. Tan, A. Banerjee, Z. Chen, Y.S. Meng, From nanoscale interface characterization to sustainable energy storage using all-solid-state batteries, Nat. Nanotechnol. 15 (3) (2020) 170.
[30] A. Manthiram, X. Yu, S. Wang, Lithium battery chemistries enabled by solid-state electrolytes, Nat. Rev. Mater. 2 (4) (2017) 16103.
[31] R. Murugan, V. Thangadurai, W. Weppner, Fast lithium ion conduction in garnet-type $Li_7La_3Zr_2O_{12}$, Angew Chem. Int. Ed. Engl. 46 (41) (2007) 7778.
[32] C. Wang, K. Fu, S.P. Kammampata, D.W. McOwen, A.J. Samson, L. Zhang, G. T. Hitz, A.M. Nolan, E.D. Wachsman, Y. Mo, V. Thangadurai, L. Hu, Garnet-type solid-state electrolytes: materials, interfaces, and batteries, Chem. Rev. 120 (10) (2020) 4257.
[33] Q. Liu, Z. Geng, C. Han, Y. Fu, S. Li, Y.-b. He, F. Kang, B. Li, Challenges and perspectives of garnet solid electrolytes for all solid-state lithium batteries, J. Power Sources 389 (2018) 120.

[34] Y. Meesala, Y.-K. Liao, A. Jena, N.-H. Yang, W.K. Pang, S.-F. Hu, H. Chang, C.-E. Liu, S.-C. Liao, J.-M. Chen, X. Guo, R.-S. Liu, An efficient multi-doping strategy to enhance Li-ion conductivity in the garnet-type solid electrolyte $Li_7La_3Zr_2O_{12}$, J. Mater. Chem. A 7 (14) (2019) 8589.
[35] H.-Y. Li, B. Huang, Z. Huang, C.-A. Wang, Enhanced mechanical strength and ionic conductivity of LLZO solid electrolytes by oscillatory pressure sintering, Ceram. Int. 45 (14) (2019) 18115.
[36] M. Müller, J. Schmieg, S. Dierickx, J. Joos, A. Weber, D. Gerthsen, E. Ivers-Tiffée, Reducing impedance at a Li-metal anode/garnet-type electrolyte interface implementing chemically resolvable in layers, ACS Appl. Mater. Interfaces 14 (12) (2022) 14739.
[37] A. Sharafi, E. Kazyak, A.L. Davis, S. Yu, T. Thompson, D.J. Siegel, N.P. Dasgupta, J. Sakamoto, Surface chemistry mechanism of ultra-low interfacial resistance in the solid-state electrolyte Li7La3Zr2O12, Chem. Mater. 29 (18) (2017) 7961.
[38] C.-L. Tsai, V. Roddatis, C.V. Chandran, Q. Ma, S. Uhlenbruck, M. Bram, P. Heitjans, O. Guillon, $Li_7La_3Zr_2O_{12}$ interface modification for Li dendrite prevention, ACS Appl. Mater. Interfaces 8 (16) (2016) 10617.
[39] S.W. Nam, D. Lee, E. Choi, J. Yeom, S.H. Choi, D.-J. Yoo, Spotlighting composite cathode heterogeneity: challenges and strategies for all-solid-state batteries, ACS Appl. Energy Mater. 8 (11) (2025) 6876.
[40] A. Bielefeld, D.A. Weber, J. Janek, Microstructural modeling of composite cathodes for all-solid-state batteries, J. Phys. Chem. C 123 (3) (2019) 1626.
[41] A. Sakuda, T. Takeuchi, H. Kobayashi, Electrode morphology in all-solid-state lithium secondary batteries consisting of $LiNi_{1/3}Co_{1/3}Mn_{1/3}O_2$ and Li_2S-P_2S_5 solid electrolytes, Solid State Ionics 285 (2016) 112.
[42] H.Y. Ko, J. Park, J.Y. Lee, Y.J. Park, Modification of cathode surface for sulfide electrolyte-based all-solid-state batteries using sulfurized $LiNbO_3$ coating, Batter. Supercaps 8 (11) (2025).
[43] J. Dhom, R. Röß-Ohlenroth, B. Stumper, C. Berger, R. Daub, Challenges and opportunities in composite cathode production of polymer-based solid-state batteries, Proced. CIRP 130 (2024) 443.
[44] J. Schnell, T. Günther, T. Knoche, C. Vieider, L. Köhler, A. Just, M. Keller, S. Passerini, G. Reinhart, All-solid-state lithium-ion and lithium metal batteries – paving the way to large-scale production, J. Power Sources 382 (2018) 160.
[45] K.J. Kim, J.L.M. Rupp, All ceramic cathode composite design and manufacturing towards low interfacial resistance for garnet-based solid-state lithium batteries, Energy Environ. Sci. 13 (12) (2020) 4930.
[46] S. Uhlenbruck, J. Dornseiffer, S. Lobe, C. Dellen, C.-L. Tsai, B. Gotzen, D. Sebold, M. Finsterbusch, O. Guillon, Cathode-electrolyte material interactions during manufacturing of inorganic solid-state lithium batteries, J. Electroceram. 38 (2-4) (2016) 197.
[47] A.A. Hubaud, D.J. Schroeder, B.J. Ingram, J.S. Okasinski, J.T. Vaughey, Thermal expansion in the garnet-type solid electrolyte $(Li_{7-x}Al_{x/3})La_3Zr_2O_{12}$ as a function of Al content, J. Alloys Compd. 644 (2015) 804.
[48] E.J. Cheng, N.J. Taylor, J. Wolfenstine, J. Sakamoto, Elastic properties of lithium cobalt oxide ($LiCoO_2$), J. Asian Ceram. Soc. 5 (2) (2017) 113.
[49] C.-L. Tsai, Q. Ma, C. Dellen, S. Lobe, F. Vondahlen, A. Windmüller, D. Grüner, H. Zheng, S. Uhlenbruck, M. Finsterbusch, F. Tietz, D. Fattakhova-Rohlfing, H. P. Buchkremer, O. Guillon, A garnet structure-based all-solid-state Li battery without interface modification: resolving incompatibility issues on positive electrodes, Sustain. Energy Fuels 3 (1) (2019) 280.
[50] A.Y. Hou, C.Y. Huang, C.L. Tsai, C.W. Huang, R. Schierholz, H.Y. Lo, H. Tempel, H. Kungl, R.A. Eichel, J.K. Chang, W.W. Wu, All-solid-state garnet-based lithium batteries at work-in operando TEM investigations of delithiation/lithiation process and capacity degradation mechanism, Adv. Sci. 10 (5) (2023) e2205012.
[51] M. Ihrig, M. Finsterbusch, A.M. Laptev, C.H. Tu, N.T.T. Tran, C.A. Lin, L.Y. Kuo, R. Ye, Y.J. Sohn, P. Kaghazchi, S.K. Lin, D. Fattakhova-Rohlfing, O. Guillon, Study of $LiCoO_2$/$Li_7La_3Zr_2O_{12}$:Ta interface degradation in all-solid-state lithium batteries, ACS Appl. Mater. Interfaces 14 (9) (2022) 11288.
[52] Z. Qin, J. Ahmed, S. Speer, D.L. Danilov, A. Windmuller, S. Yu, C.L. Tsai, H. Tempel, J. Granwehr, W.W. Wu, J.K. Chang, R.A. Eichel, P.H.L. Notten, Impact of oxygen vacancies in $LiCoO_2$ on the electrochemical performance of garnet-based all-solid-state Li-Metal batteries, Adv. Sci. (Weinh.) 12 (39) (2025) e08750.
[53] K. Hara, T.A. Yano, K. Suzuki, M. Hirayama, T. Hayashi, R. Kanno, M. Hara, Raman imaging analysis of local crystal structures in $LiCoO_2$ thin films calcined at different temperatures, Anal. Sci. 33 (7) (2017) 853.
[54] C.H. Toni Gross, Raman diagnostics of $LiCoO_2$ electrodes for lithium-ion batteries, J. Power Sources 256 (2014) 220.
[55] S.K. Tripathy, M. Christy, N.-H. Park, E.-K. Suh, S. Anand, Y.-T. Yu, Hydrothermal synthesis of single-crystalline nanocubes of Co_3O_4, Mater. Lett. 62 (6) (2008) 1006.
[56] N. Janani, C. Deviannapoorani, L. Dhivya, R. Murugan, Influence of sintering additives on densification and Li^+ conductivity of Al doped $Li_7La_3Zr_2O_{12}$ lithium garnet, RSC Adv. 4 (93) (2014) 51228.
[57] L. Dhivya, R. Murugan, Effect of simultaneous substitution of Y and Ta on the stabilization of cubic phase, microstructure, and Li+ conductivity of $Li_7La_3Zr_2O_{12}$ Lithium garnet, ACS Appl. Mater. Interfaces 6 (20) (2014) 17606.
[58] G. Larraz, A. Orera, M.L. Sanjuán, Cubic phases of garnet-type $Li_7La_3Zr_2O_{12}$: the role of hydration, J. Mater. Chem. A 1 (37) (2013) 11419.
[59] T. Thompson, J. Wolfenstine, J.L. Allen, M. Johannes, A. Huq, I.N. David, J. Sakamoto, Tetragonal vs. cubic phase stability in Al-free Ta doped $Li_7La_3Zr_2O_{12}$ (LLZO), J. Mater. Chem. A 2 (33) (2014) 13431.
[60] M.H. Brooker, J.B. Bates, Raman and infrared spectral studies of anhydrous Li_2CO_3 and Na_2CO_3, J. Chem. Phys. 54 (11) (1971) 4788.
[61] M. Rosen, R. Ye, M. Mann, S. Lobe, M. Finsterbusch, O. Guillon, D. Fattakhova-Rohlfing, Controlling the lithium proton exchange of LLZO to enable reproducible processing and performance optimization, J. Mater. Chem. A 9 (8) (2021) 4831.
[62] W.S. Scheld, K. Kim, C. Schwab, A.C. Moy, S.K. Jiang, M. Mann, C. Dellen, Y. J. Sohn, S. Lobe, M. Ihrig, M.G. Danner, C.Y. Chang, S. Uhlenbruck, E. D. Wachsman, B.J. Hwang, J. Sakamoto, L.F. Wan, B.C. Wood, M. Finsterbusch, D. Fattakhova-Rohlfing, The riddle of dark LLZO: cobalt diffusion in garnet separators of solid-state lithium batteries, Adv. Funct. Mater. 33 (43) (2023).
[63] H.-C. Yu, D. Taha, T. Thompson, N.J. Taylor, A. Drews, J. Sakamoto, K. Thornton, Deformation and stresses in solid-state composite battery cathodes, J. Power Sources 440 (2019) 227116.
[64] S. Han, D. Kil, S. Lee, H. Park, K.-h. Ko, W. Kim, J. Park, C. Lim, K. Yoon, J. Noh, D. Eum, D. Won, K. Kang, A full oxide-based solid-state lithium battery and its unexpected cathode degradation mechanism, ACS Energy Lett. 8 (11) (2023) 4794.
[65] M.M.U. Din, L. Ladenstein, J. Ring, D. Knez, S. Smetaczek, M. Kubicek, M. Sadeqi-Moqadam, S. Ganschow, E. Salagre, E.G. Michel, S. Lode, G. Kothleitner, I. Dugulan, J.G. Smith, A. Limbeck, J. Fleig, D.J. Siegel, G.J. Redhammer, D. Rettenwander, A guideline to mitigate interfacial degradation processes in solid-state batteries caused by cross diffusion, Adv. Funct. Mater. 33 (42) (2023).